RESEARCH

Heteroatoms doped iron oxide-based catalyst prepared from zinc slag for efficient selective catalytic reduction of NO$_x$ with NH$_3$

Jiale Liang[1] · Yaojun Zhang[1] · Hao Chen[2] · Licai Liu[1] · Panyang He[3] · Lei Wu[2]

Abstract

Excessive emissions of nitrogen oxides from flue gas have imposed various detrimental impacts on environment, and the development of deNO$_x$ catalysts with low-cost and high performance is an urgent requirement. Iron oxide-based material has been explored for promising deNO$_x$ catalysts. However, the unsatisfactory low-temperature activity limits their practical applications. In this study, a series of excellent low-temperature denitrification catalysts (Ha-FeO$_x$/yZS) were prepared by acid treatment of zinc slag, and the mass ratios of Fe to impure ions was regulated by adjusting the acid concentrations. Ha-FeO$_x$/yZS showed high denitrification performance (> 90%) in the range of 180–300 °C, and the optimal NO conversion and N$_2$ selectivity were higher than 95% at 250 °C. Among them, the Ha-FeO$_x$/2ZS synthesized with 2 mol/L HNO$_3$ exhibited the widest temperature window (175–350 °C). The excellent denitrification performance of Ha-FeO$_x$/yZS was mainly attributed to the strong interaction between Fe and impurity ions to inhibit the growth of crystals, making Ha-FeO$_x$/yZS with amorphous structure, nice fine particles, large specific surface area, more surface acid sites and high chemisorbed oxygen. The in-situ DRIFT experiments confirmed that the SCR reaction on the Ha-FeO$_x$/yZS followed both Langmuir-Hinshelwood (L-H) mechanism and Eley-Rideal (E-R) mechanism. The present work proposed a high value-added method for the preparation of cost-effective catalysts from zinc slag, which showed a promising application prospect in NO$_x$ removal by selective catalytic reduction with ammonia.

Keywords Flue gas · NO$_x$ removal · Zinc slag-derived catalyst · NH$_3$-SCR · Catalysis activity

1 Introduction

Nitrogen oxides are one of the most common contributors to atmospheric pollution. The majority of these emissions are caused by the fossil fuels combustions, such as in coal-fired power plants or the diesel engines of cars and trucks (Luo et al. 2022; Shan et al. 2016), which has caused many environmental issues (Zhu et al. 2022; Qi et al. 2020; Awual et al. 2019; Awual 2016). Selective catalytic reduction (SCR) of NO$_x$ with ammonia is currently the most imperative, successful, and commercially applicable method for NO$_x$ removal (Twigg 2007; Pu et al. 2022). Iron-based oxides are recognized as a kind of efficient SCR catalysts in industrial applications because of their low toxicity, high reactivity and satisfactory N$_2$ selectivity (Han et al. 2019a, b). Unfortunately, the SCR reactivity of pure iron oxide-based catalysts at low temperatures (LT) is not satisfied owing to the lack of acid sites and redox capabilities (Mu et al. 2020). Numerous attentions have been attached on regulating the crystalline phase /facet structures and nanostructures of iron oxides, or doping heteroatoms into the oxide matrix so that improve the oxidizing ability and acidity/redox properties of catalysts (Han et al. 2019a, b). Nevertheless, how to produce Fe-based SCR catalyst with simpler method and low-cost is still challenging (Han et al. 2019a, b).

Zinc slag (ZS), which is also called as lead-zinc slag, or ferro-silicate slag (FSG) (Morrison et al. 2003), is the primary solid waste produced during the zinc ore smelting

✉ Yaojun Zhang
  zhangyaojun@xauat.edu.cn

1 College of Materials Science and Engineering, Xi'an University of Architecture and Technology, Xi'an 710055, China

2 School of Chemistry and Chemical Engineering, Xi'an University of Architecture and Technology, Xi'an 710055, China

3 School of Resources Engineering, Xi'an University of Architecture and Technology, Xi'an 710055, China

processes. In recent years, the global metal zinc consumption has exceeded 13 million tons per year, which is inevitably accompanied by the increase in ZS discharge (Song et al. 2019) and the issue of ZS disposal has not been properly solved. Recently, Nath et al. (Nath 2020) reported the preparation geopolymer paving blocks using ZS/fly ash blends as raw materials. Xia et al. (Xia et al. 2019) investigated the solidification/stabilization of ZS by preparing of geopolymer composites. There are also some other similar reported works, which all highlight the harmless utilization potential of ZS in construction and building materials areas (Zhang et al. 2022; Pan et al. 2019). Nevertheless, it is still wasteful to use ZS as building materials because large amounts of useful elements such as Fe and Mn in ZS are not sufficiently used with high added value. Indeed, ZS contains approximately 35 wt% Fe_2O_3 and a small amount of other metal oxides (Nath 2020; Alex et al. 2013; Prasad et al. 2016). Hence, if the active components in zinc slag could be extracted and enriched producing nanocomposite material(Awual 2016, 2017; Awual et al. 2017a, b; Awual 2019), zinc slag would become potential raw to prepare environment remediation materials with high added value, e.g. composite Fe-based catalyst for the treatment of wastewater or waste gas (Zhang et al. 2013; Chen et al. 2023; Li et al. 2021; Awual et al. 2017a, b, 2019).

Herein, ZS was utilized as the sole raw material to prepare novel low-cost and high-performance iron oxide-based deNO$_x$ catalyst by extracting and restructuring of the endogenous constituents of ZS. This idea is based on following considerations:(1) ZS is a kind of solid waste, but it contains a considerable high iron content (greater than 35 wt%), which can be extracted and enriched under acidic condition. (2) Except for iron species, some other acid soluble elements such as Al and Mn also exist in ZS, which can be extracted simultaneously during the solation process. These elements can be utilized as heteroatoms doped in FeO$_x$ catalyst matrix to promote nanocomposite material producing. (3) This method allows the preparation of structure controllable and analyzable iron oxide-based deNO$_x$ catalyst, which has weighty significance for zinc slag utilization in large-scale.

In the present work, zinc slag was dissolved by different concentrations of HNO$_3$ to control the extraction rate of different elements, and followed by precipitation and calcination to prepare heteroatoms doped iron oxide-based SCR catalysts. The changes in the pore structure, crystalline structure, surface texture, redox capability, chemical components, and microtopography under different acid concentrations are systematically evaluated via various spectroscopy methods, and the changes are also compared with their variation in SCR reactivities. Moreover, a pure Fe_2O_3 was also prepared using chemical reagent under the same condition as comparison, so that better protrude the superiority and advancement of the iron oxide-based catalyst derived from low-cost zinc slag waste.

2 Materials and methods

2.1 Catalyst synthesis

Raw zinc slag (ZS) was provided by Shanxi Shangluo Lead-zinc smelter, which was directly used without further purification. Nitric acid (65 wt%), analytic pure reagents including ion nitrate nonahydrate, aluminum nitrate nonahydrate, silica sol, magnesium nitrate hexahydrate calcium chloride, zinc nitrate hexahydrate, and manganese nitrate hydrate, and ammonium hydroxide (25 wt%) were provided by Sinopharm Chemical Reagent Co., Ltd.

ZS-derived catalysts (Ha-FeO$_x$/yZS) were synthesized by the sol-gel method. Firstly, raw was dried and ground to pass 0.154 mm sieve, and then dissolved 10 g of raw material in y mol/L ($y=0.5$, 2.0, 4.0, 6.0) of HNO$_3$ solution at 75 °C for 6 h to extract metal ions. The mass ratio of solid/liquid was 1:30. Subsequently, ammonia hydroxide was added dropwise into the mixture solution for adjusting the pH value to approximately 9 and transforming the mixture solution from sol to gel via stirring for several hours. Then, the obtained gel was filtered and separated, and washed for 3–5 times ensuring the pH of the gel was around 7. Thereafter, the gel was dried in an oven (105 °C, 12 h) before being calcined in a muffle furnace (400 °C, 5 h). The FeO$_x$ sample was also prepared via sol-gel method under the same condition to study the effect of heteroatoms on the structure and morphology of the samples.

2.2 Catalytic experiments

The performance testing experiments were carried out in a quartz reactor (inner diameter: 6 mm). In each run, 0.4 g of catalyst was put into the reactor with pretreatment at 450 °C for half an hour. After cooling the reactor to 80 °C, the gas mixture was injected into the reaction cell at 168 mL/min (NO = NH$_3$ = 750 ppm; 5 vol% O$_2$; GHSV = 20,000 h^{-1} balanced by N$_2$). The outlet gas concentration was recorded every 25 °C interval for 30 min from 125 to 450 °C to assess the NO conversion of the catalysts. The NO$_x$ conversion and N$_2$ selectivity are calculated by equations below (Pu et al. 2022):

$$\text{NO conversion} = \left(1 - \frac{[NO_x]_{out}}{[NO_x]_{in}} \right) \times 100\% \tag{1}$$

$$N_2 \, \text{selectivity} = \left(1 - \frac{2[N_2O]_{out}}{[NO]_{in} + [NH_3]_{in} - [NO]_{out} - [NH_3]_{out}}\right) \times 100\% \quad (2)$$

The $[NO_x]_{in}$ is inlet NO_x concentrations; $[NO_x]_{out}$ is outlet NO_x concentrations; while $[NH_3]_{in/out}$ is inlet or outlet NH_3 concentrations, respectively.

2.3 Characterizations

The chemical components of the samples were quantitatively analyzed by X-ray fluorescence (XRF) using an ARL PERFORM'X Analyzer. The crystalline structure of the samples was detected by Rigaku D/Max 2200 X-ray diffractometer (XRD) at 40 kV and 26 mA. Raman spectrum was recorded on the LabRAM HR Evolution spectrometer using a 532 nm laser beam. SEM and TEM images were observed by a Sigma-300 scanning electron microscope (Zeiss, Germany) and a JEOL JEM-2100 F field-emission electron microscopy at 200 kV. Micrometrics APSP 2460 analyzer was utilized to recorded the gas adsorption isotherm for further calculating the BET surface areas as well as the pore size distributions. Thermo SCIENTIFIC ESCALAB Xi+equipment was used for analyzing the surface state of the catalysts.

H_2-TPR and NH_3-TPD experiments were carried out on a completely automatic chemical adsorption device (Auto Chem TM II 2920, Micromeritics, USA). For H_2-TPR: catalysts were preheated in a helium flow (300 °C, 1 h) and then heated to 800 °C at 10 °C/min in 10% H_2/He (50 mL/min). For NH_3-TPD: catalysts were placed in a reaction tube

and firstly heated with helium flow (300 °C, 1 h). After the catalyst cooled to 50 °C, a flow of 10% NH_3/He (50 mL/min) was fed in until the equilibrium of adsorption, and then heated to 800 °C at 10 °C/min.

VERTEX 70v was utilized for observing the in-situ DRIFTS spectra. Catalysts were first processed in N_2 (350 °C, 30 min) flow to remove impurity substances and then cooled to 250 °C. Then, a gas mixture (NH_3 or $NO + O_2$) was introduced into catalyst surface for 30 min, purged with N_2, and reacted with the flow of NH_3 or $NO + O_2$. The IR curves were recorded at intervals and analyzed in order to comprehend the SCR catalytic mechanism.

3 Results and discussion

3.1 SCR performance

Figure 1a compares the catalytic performance of ZS, FeO_x and Ha-FeO_x/2ZS samples. Owing to the presence of abundant iron and other metal species, ZS sample exhibits SCR reactivity, where the NO conversion slowly increased in 125–425 °C and then decreased. However, the highest NO conversion of ZS is only approximately 78% at a high temperature of 375 °C, and it is almost inactive at LT (less than 250 °C), suggesting that ZS is not suitable directly utilized for NO_x removal, which requires a further treatment. Meanwhile, FeO_x sample exhibits approximately 65% NO conversion at around 300 °C and the change of conversion rate

Fig. 1 a Catalytic activity of ZS, FeO_x and Ha-FeO_x/2ZS catalysts **b** Catalytic activity of Ha-FeO_x/yZS catalysts **c** N_2 selectivity of Ha-FeO_x/yZS catalyst **d** stability of Ha-FeO_x/2ZS at 250 °C (NO = NH_3 = 750 ppm; O_2 = 5 vol%; balance N_2; GHSV = 20,000 h^{-1})
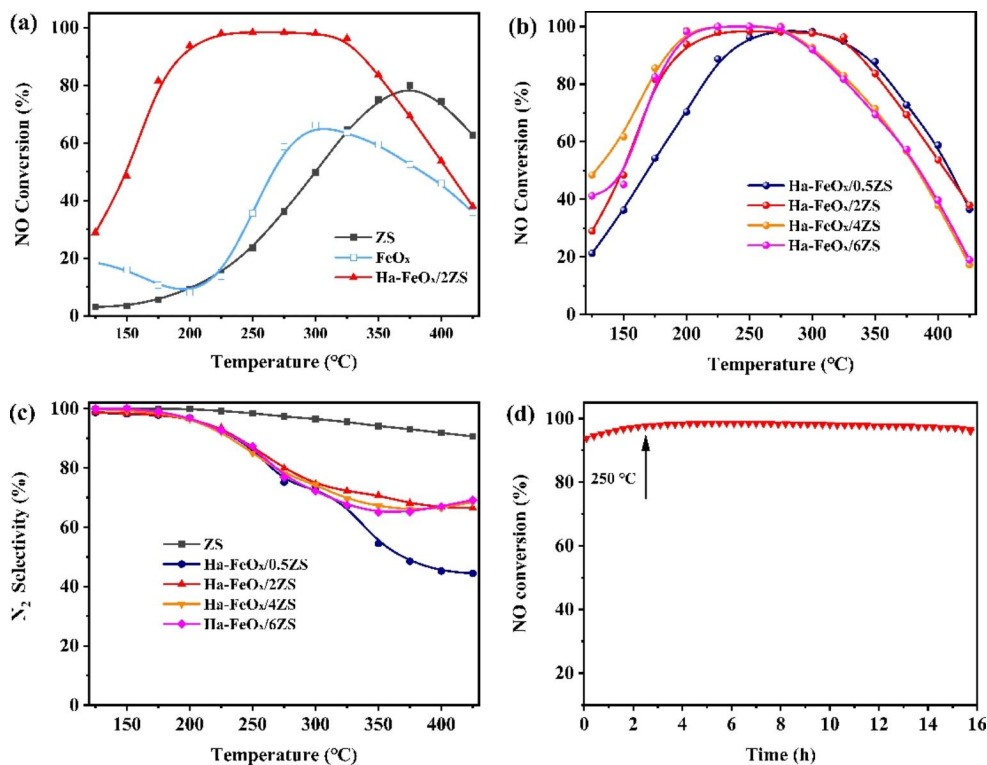
with temperature is similar to the ZS. Notably, following by recombining the active contents from zinc slag, the NO conversion over Ha-FeO$_x$/2ZS is obviously increased which means that the new synthesized catalyst could maintain excellent catalytic performance (> 90%) in the temperature range of 190–340 °C.

As shown in Fig. 1b, the ZS-derived catalysts prepared under different nitric acid conditions all show better SCR performance than that of zinc slag, especially at low temperatures. When ZS was treated under low acid concentration, the NO conversion of the Ha-FeO$_x$/0.5ZS was 90% at 225 °C, and up to 96% at 275–300 °C. Although the NO conversion of Ha-FeO$_x$/0.5ZS gradually decreases with the rising of the temperature, it remains at a high value of approximately 88% at 350 °C, higher than that of raw ZS. Furthermore, when ZS was treated under higher acid concentrations, the NO conversion is further enhanced, whereas the temperature window showed an increasing trend first and then declined. Ha-FeO$_x$/2ZS exhibits the widest reaction temperature window. Its NO conversion reached up to 82% and N$_2$ selectivity was nearly 100% at 170 °C (Fig. 1c). The conversion ratio further increased above 90% at elevated temperatures (190–325 °C). According to Figure S1, Ha-FeO$_x$/2ZS also performed well at different GHSV. Although the GHSV went up to 80,000 h^{-1}, the activity was only decreased from 98.4 to 89.2% at 250 °C. Moreover, the ZS-derived catalysts had excellent LT SCR reactivity and wide working temperature ranges when comparing with other reported catalysts (Table 1).

3.2 Physical properties

Table S1 summaries the chemical components of raw ZS and ZS-derived catalysts. It is clear that ZS is predominately made up of Fe, Si, Al and Ca species, Especially, the Fe species account for half of the original amount. Other metal species such as Mn, Zn, Mg, etc. are less than 5%. However, the amount of iron species in the Ha-FeO$_x$/yZS catalyst significantly grew from 49.34% to 73.36% with the increase of acidic concentration. In contrast, the amount of Si species indicated a decreasing trend because of the insoluble quartz existing. In a word, after the acid extraction and alkali precipitation treatment (Fig. 2a), the main elemental compositions of the obtained catalysts are similar to that of ZS, but they are essentially different among crystalline structure, microtopography, and physicochemical property.

As shown in Fig. 2b, the raw ZS exhibits a condensed bulk morphology with some cracks that formed during the slag collection process. Figure 2c displays the microstructure of pure FeO$_x$, and we can see that the iron oxides are well crystalized with a particle size of approximately 30 nm, and these regular multilateral particles are packing

closely. However, the Ha-FeO$_x$/yZS catalyst as shown in Fig. 2d exhibits an amorphous morphology, and the catalyst particles are accumulated by smaller nanoparticles with particle size of approximately 5–10 nm. Moreover, the interconnected accumulation of these refined nano-sized particles naturally forms abundant pore structures, which would facilitate the SCR reaction.

Figure 3a displayed the XRD patterns of different catalysts, where we could see that ZS exhibited a broad diffraction peak coupled with some sharp ones. In reported literatures, the broad hump peak at approximately 20°–40° 2θ was regarded as amorphous aluminosilicate (Chen et al. 2019), while these sharp peaks at 35.4, 43.0 and 53.4 are ascribed to (311), (400) and (422) surfaces of quartz (JCPDS NO.46-1045), crystalline magnetite (JCPDS NO.74–0748) and mullite (JCPDS NO.31–0267), respectively.

Differently, as shown in Fig. 3a and Figure S2, all the samples treated with different acid concentrations exhibited two broad hump peaks centered at approximately 35° and 62°, which are the characteristic peaks of amorphous Fe$_2$O$_3$ doped with heteroatoms. Zhang et al.(Zhang et al. 2021a, b) and Sun et al.(Sun et al. 2017) demonstrated that the doping ions lead to the formation of poorly crystalline Fe$_2$O$_3$. As a comparison, we can see that the pure FeO$_x$ prepared from chemical reagent under the same condition displays clear diffraction peaks, where the peaks at 24.1°, 33.1°, 35.6°, 40.8°, 49.4°, 54.0°, 57.4°, 62.4°, 64.0°, and 71.9° 2θ are consistent well with (012), (104), (110), (113), (024), (116), (122), (214), (300) and (1010) crystalline surfaces of hematite Fe$_2$O$_3$. These results suggest that the impurity elements from ZS would greatly affect the crystal growth of Fe$_2$O$_3$. Indeed, previous works have also shown that the doping of cations such as Si, Al, Ti, and Ce into the FeO$_x$ matrix would significantly induce the deformation of FeO$_x$ unit cell and suppresses crystal growth, thereby reducing the particle size and results in amorphous phase product (Sun et al. 2017). Notably, poor crystallized FeO$_x$ was more efficient in SCR reaction because it had better pore structure and more exposed active sites (Zhang et al. 2021a, b).

Raman spectra of the ZS, Ha-FeO$_x$/2ZS and FeO$_x$ were shown in Fig. 3b. ZS had three mainly large peaks at 370, 520 and 670 cm^{-1}, which were considered as the magnetite phase in raw ZS (Chernyshova et al. 2007; Bersani et al. 1999). For pure FeO$_x$, peaks at 225 (A$_{1g}$), 245 (E$_g$), 411 (E$_g$), 504(A$_{1g}$), and 611 (E$_g$) cm^{-1} ascribed to α-Fe$_2$O$_3$ were clearly observed (Faria et al. 2005). What is worth highlighting, however, is that the peak related to the α-Fe$_2$O$_3$ shows significantly weaker and wider for Ha-FeO$_x$/2ZS catalyst with an emerging shoulder peak at 611 cm^{-1} (Chernyshova et al. 2007), which reveals the presence of the poorly crystallized Fe$_2$O$_3$ nanoparticles, as demonstrated in Figs. 2d and 3a.

Table 1 The reactivity of various iron-based catalysts

Sample	Reaction condition (N_2 balance)				Precursors	Preparation method	NO removal conversion (%)
	NO (ppm)	NH_3 (ppm)	O_2 (vol%)	GHSV (h^{-1})			
Ha-FeO$_x$/2ZS	750	750	5	20,000	Zinc slag	sol-gel	90%–100% (190–340 °C)
Mn$_{(0.2)}$-FeO$_x$ (Li et al. 2016)	500	500	5	30,000	$FeCl_3 \cdot 6H_2O$ $Mn(NO_3)_2 \cdot 2H_2O$	co-precipitation	90%–100% (230–400 °C)
FeW(5) (Li et al. 2015)	500	500	5	60,000	$Fe(NO_3)_3 \cdot 9H_2O$ $(NH_4)_6W_7O_{24} \cdot 6H_2O$	co-precipitation	97% (250–400 °C)
MnO$_x$-FeO$_x$ nanoneedles (Fan et al. 2017)	500	500	5	36,000	$Fe(NO_3)_2 \cdot 9H_2O$ $Mn(NO_3)_2 \cdot 4H_2O$	hydrothermal	95%–100% (90–260 °C)
Mn$_{0.5}$Fe$_{2.5}$O$_4$-S (Wei et al. 2020)	500	500	5	25,000	$Fe(NO_3)_3 \cdot 9H_2O$ $Mn(NO_3)_2 \cdot 6H_2O$	solvothermal	≥90% (90–300 °C)
Fe$_9$Ti$_1$O$_x$ (Sun et al. 2017)	500	500	5	60,000	$Fe(NO_3)_2 \cdot 9H_2O$ $Ti(SO_4)$	coprecipitation	≥80% (150–350 °C)
10% Mn/Fe-Ti spinel (Yang et al. 2016)	500	500	2	24,000	manganese nitrate Fe-Ti spinel	co-precipitation and impregnation	95%–100% (150–250 °C)
Fe$_2$O$_3$-H$_2$SO$_4$ (Zhang et al. 2018)	600	600	3	72,000	Fe_2O_3 oxides	impregnation	≥90% (320–440 °C)
Fe/Beta (Liu et al. 2017a, b)	500	500	3	125,000	$NaAlO_2$ $Fe(NO_3)_2 \cdot 9H_2O$	incipient-wetness impregnation	≥80% (260–510 °C)
γ-Fe$_2$O$_3$ (Yu et al. 2021)	500	500	5	60,000	γ-Fe_2O_3	-	70%–90% (200–300 °C)
α-Fe$_2$O$_3$ (Liu et al. 2017a, b)	500	500	3	72,000	α-FeOOH	thermal treatment	80%–95% (300–400 °C)
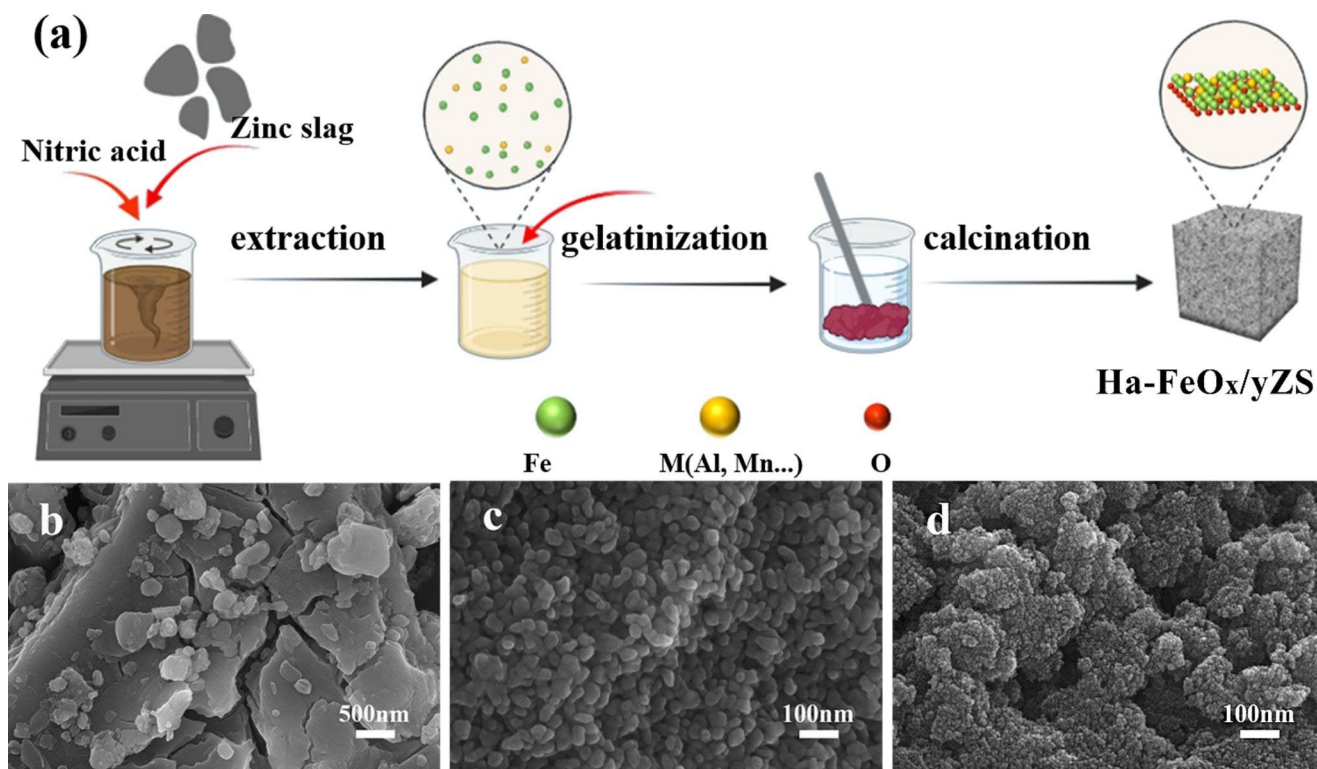
Fig. 2 **a** The procedure for the preparation of Ha-FeO$_x$/yZS catalysts via sol-gel method; FESEM image of **b** Raw ZS, **c** FeO$_x$ and **d** Ha-FeO$_x$/2ZS

Fig. 3 **a** XRD pattern and **b** Raman spectra of ZS, Ha-FeO$_x$/2ZS and FeO$_x$ samples
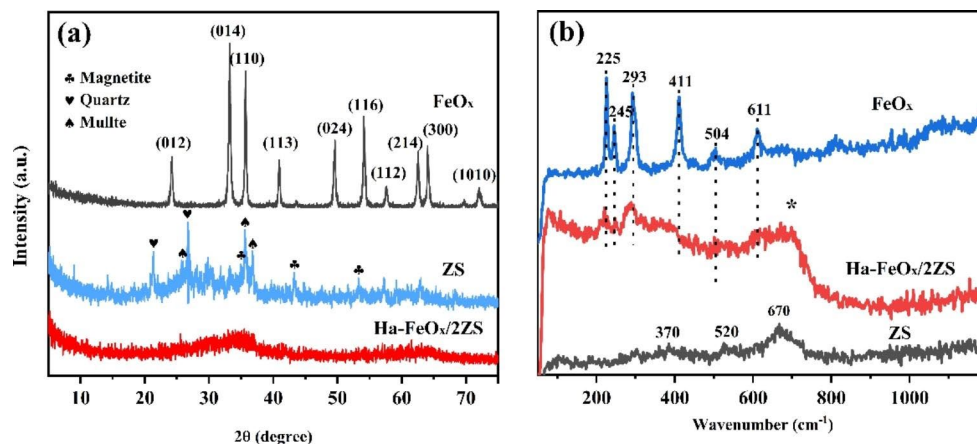

From Fig. 4a, ZS was composed of nano particles, which should be the aggregation of oxides such as magnetite, quartz and mullite as revealed by XRD. Moreover, owing to the high content of iron species, the crystalline Fe$_3$O$_4$ can be observed in raw ZS as shown in Fig. 4d. Figure 4b and e exhibited the TEM images of pure FeO$_x$, where we can see that the FeO$_x$ is well crystalized Fe$_2$O$_3$ structure with particle size of approximately 30 nm. Figure 4c and f displayed the TEM results of Ha-FeO$_x$/2ZS, where we can see that the Ha-FeO$_x$/2ZS has consisted of nanoparticles at 5–10 nm, smaller than that of pure FeO$_x$. Moreover, the high-resolution image as illustrated in Fig. 4f confirms that the nano particles are mainly amorphous, and the amorphous

structure also indicates its excellent SCR reactivity(Hasan et al. 2023a, b; Zhang et al. 2021a; Zhang et al. 2021b). Furthermore, the EDS mapping of ZS-derived catalyst as shown in Fig. 4g–n demonstrated that except for Fe, there are also some heteroatoms exist in the catalyst, and these elements are uniformly distributed in catalyst matrix, which should be the key factor responding for the as-prepared catalyst's unique structure and catalytic behavior.

Figure 5 and Figure S3 display the N$_2$ adsorption-desorption isotherms and pore size distributions of the samples, while the parameters are shown in Table 2. As shown in Fig. 5a, the plot of ZS was a type IV isotherm with a wide hysteresis loop at mid-high relative pressure ranges

Fig. 4 TEM results of **a**, **d** Raw ZS, **b**, **e** Pure FeO$_x$, **c**, **f** Ha-FeO$_x$/2ZS; the elements mapping of Ha-FeO$_x$/2ZS for Fe, O, Si, Al, Mn, Zn, and Ca (**h-n**)
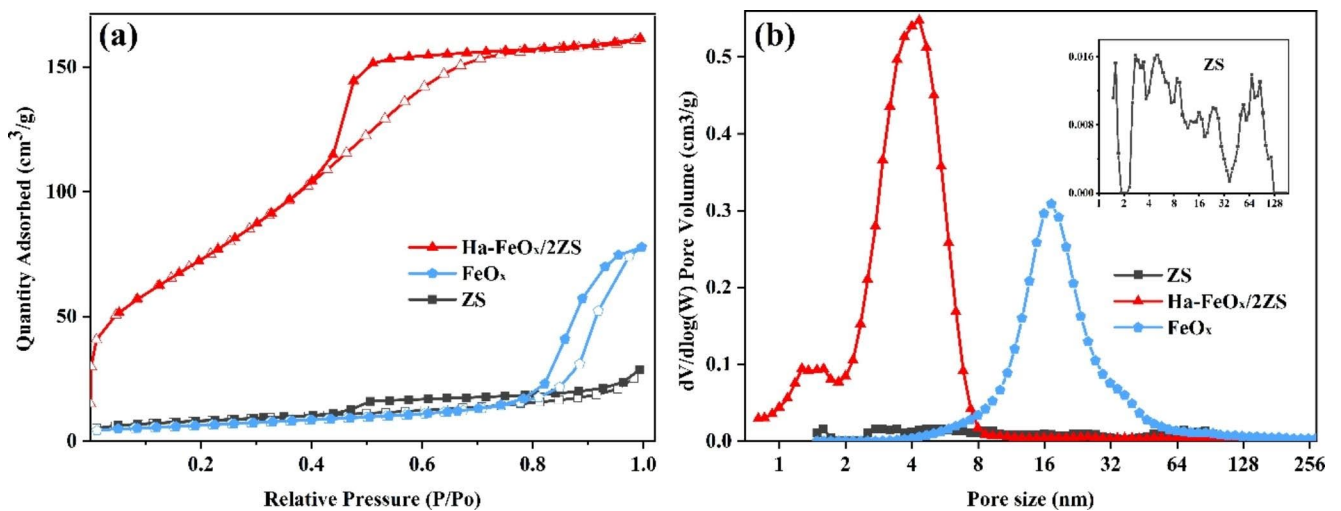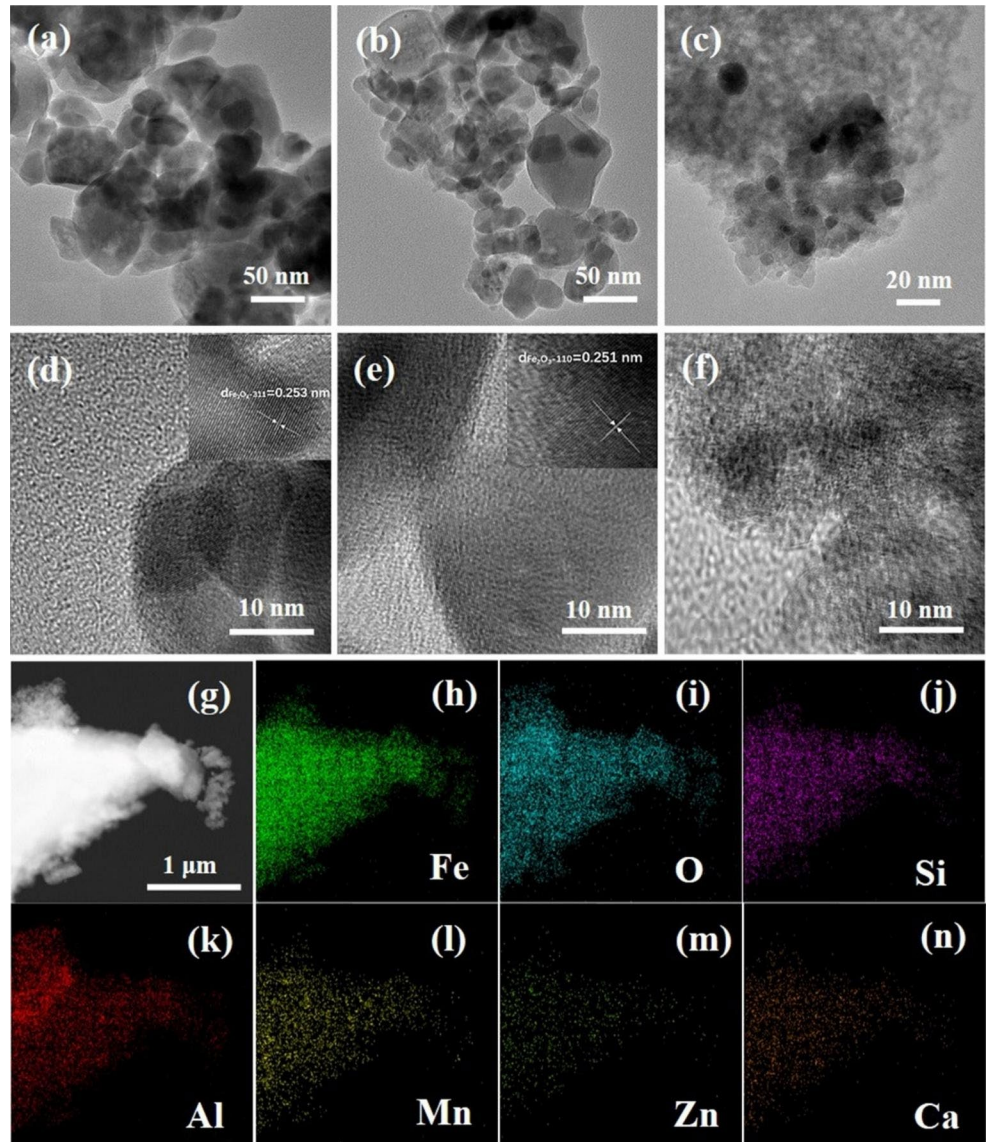
Fig. 5 **a** N$_2$ adsorption-desorption isotherms **b** Differential pore size distributions of ZS, FeO$_x$, Ha-FeO$_x$/2ZS catalysts

Table 2 Structural characteristics of catalysts

| Sample	BET surface area (m²/g)	$D_{average}$ (nm)	Pore volume (cm³/g)		
			< 2 nm	2–50 nm	> 50 nm
ZS	28.1456	4.5477	0.005	0.013	0.003
FeO$_x$	22.3422	18.5622	0.001	0.112	0.006
Ha-FeO$_x$/0.5ZS	201.4039	3.8126	0.029	0.146	0
Ha-FeO$_x$/2ZS	278.0088	3.5429	0.037	0.188	0
Ha-FeO$_x$/4ZS	228.6549	3.8256	0.028	0.172	0
Ha-FeO$_x$/6ZS	209.2006	3.7035	0.026	0.152	0.001

of 0.42–0.98 (P/P_0) (Chen et al. 2022), and the N$_2$ uptake amount was very limited, suggesting its poor developed pore structures, where the pore size distribution was dispersive, and the BET surface area was only 28 m²/g. In contrast, as illustrated in Fig. 5a and Figure S3a, all the resultant catalysts obtained under different acid conditions exhibit type IV isotherms, and the N$_2$ adsorption amounts are significantly larger than raw ZS, suggesting their well-developed hierarchical pore structure characteristics (Chen et al. 2019). As shown in Fig. 5b and Figure S3b, the ZS-derived catalysts are composed of both micropore and mesopore centered at approximately 1.4 and 3.8 nm, respectively, and the mesopores are predominant, which would promote the transformation of the reactants during the reaction, thereby facilitating the SCR reactivity. Moreover, as a comparison, we can see from Fig. 5a; Table 2 that the pure FeO$_x$ exhibits much poorer pore structure than that of ZS-derived catalyst. These results further confirm that the endogenous

heteroatoms in ZS can not only regulate the crystalline structure of the ZS-derived catalyst, but also significantly optimize its pore structures, which responses to its excellent SCR performance (Chen et al. 2011; Salman et al. 2023).

3.2.1 Surface chemical states analysis

XPS spectra was measured for further understanding the composition and state of the catalysts' surface elements. As illustrated in Fig. 6a and Figure S4, the O 1s XPS spectra was split into three independent peaks located at 529.3–530.2, 530.9–532.0 eV and 533.0-533.4 eV. The band at lower binding energy was lattice oxygen O′ species (O^{2-}), and the higher represented for chemisorbed oxygen O″ species, including the surface oxygen vacancy (O_2^{2-}, O_2^-) and adsorbed water, respectively (Wei et al. 2020; Liu et al. 2010; Liu et al. 2021a, b). O″ was more active in the oxidizing process because they have higher mobilities than lattice oxygen species (O′) (Kang et al. 2021); besides, the adsorbed chemisorbed oxygen O″ species can effectively promote the oxidation of NO (Fang et al. 2022), and the redox cycle of active substances, thereby facilitating the SCR reactivity of samples (Liu et al. 2021a, b; Sheng et al. 2018). In Table 3; Fig. 6a, all the ZS-derived catalysts exhibit high chemisorbed oxygen O″ species above 72%, which are much higher than that of pure FeO$_x$ (28.04%). The biggest difference between ZS-derived iron oxide-based catalysts and pure FeO$_x$ is their chemical components. As shown in

Fig. 6 XPS patterns of **a** O 1s; **b** Fe 2p of the ZS, Ha-FeO$_x$/2ZS and FeO$_x$ catalysts
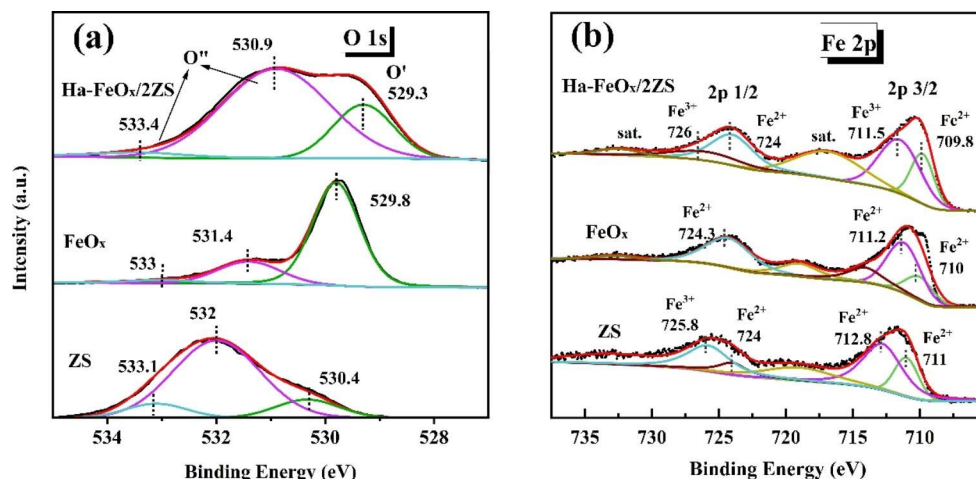
**Table 3** Atomic concentrations and relative ratios of the main elements

Sample	Atomic concentration (%)						Relative concentration (%)	
	O	Fe	Mn	Al	Si	Ca	O″/(O″ + O′)	Fe²⁺/(Fe²⁺ + Fe³⁺)
FeO$_x$	54.48	28.71	-	-	-	-	28.04	16.92
ZS	67.17	9.27	0.92	8.75	11.14	2.72	70.14	28.12
Ha-FeO$_x$/0.5ZS	69.06	8.22	1.60	6.44	9.34	5.31	73.98	35.86
Ha-FeO$_x$/2ZS	66.10	14.79	1.51	7.57	8.39	1.61	81.05	50.00
Ha-FeO$_x$/4ZS	66.36	15.81	1.84	8.94	4.90	2.12	73.26	51.42
Ha-FeO$_x$/6ZS	64.47	19.35	1.85	9.62	2.92	1.76	72.86	45.50

Table 3, except for iron species, a small amount of impurity cations such as Si, Al, and Mn are also present in ZS-derived catalysts' surface. Combining with above XRF, XRD, BET, Raman, and microtopography results, it can be certified that the impurity atoms that simultaneously extracted during the acid treatment of ZS can effectively inhibit the growth of iron oxide, which not only improve pore structure of iron oxide-based catalysts, but also increase its adsorbed oxygen content, thereby improving its SCR reactivity.

Furthermore, these heteroatoms can also improve the redox property of iron oxide-based catalyst. In general, higher Fe^{2+} content in iron oxide-based catalyst indicates better redox capability (Zhang et al. 2020; Yuan et al. 2022; Wang et al. 2020). However, for a pure FeO_x catalyst, as shown in Fig. 6b and Table 3, owing to its well-developed crystalline structure, it is mainly composed of Fe^{3+}, where the Fe^{2+} proportion is only approximately 16.92%. This should be one of the crucial underlying causes that pure FeO_x catalyst exbibits poor SCR reactivity. In contrast, the Fe^{2+} contents in ZS-derived catalysts are 2 to 3 times larger than that of pure FeO_x, which should be attributed the influence of impure heteroatoms. Indeed, Sun et al. (Sun et al. 2017) analyzed the influence of doping with heteroatoms on the Fe^{2+} content of iron oxide-based catalysts. Their results confirmed that the strong interaction among the doped cations and Fe species would regulate the inherent electron cloud of iron atoms, which promotes the formation of more Fe^{2+} species, thereby facilitating the redox property of samples, and further enhance SCR reactivity.

3.2.2 H_2-TPR

Herein, H_2-TPR experiments were performed to better understand the redox properties of samples. Based on previous studies, the reduction of pure Fe_2O_3 with H_2 could take place in the following order: $Fe_2O_3 \rightarrow Fe_3O_4 \rightarrow FeO \rightarrow Fe$ with
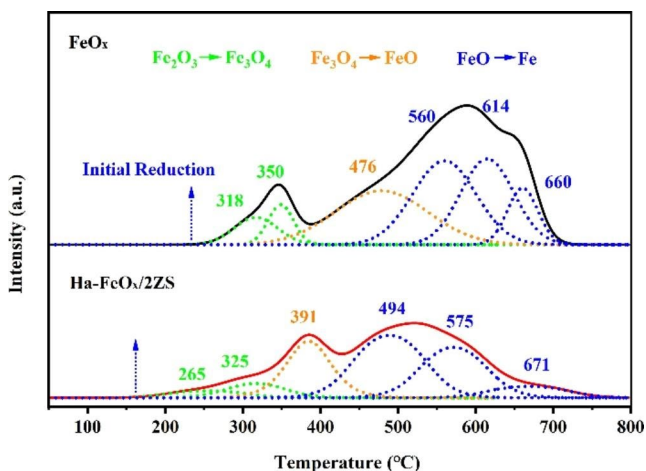

Fig. 7 H_2-TPR patterns of FeO_x and Ha-FeO_x/2ZS samples

a hydrogen molar ratio of 1:2:6 (Zhang et al. 2021a, b; Liu et al. 2021a, b). According to this ratio, the H_2-TPR profiles of pure FeO_x and ZS-derived catalysts were divided into three steps with increasing temperatures as shown in Fig. 7, Figure S5, and Table S2. In Fig. 7, the reduction temperature of pure Fe_2O_3 to Fe_3O_4 was centered at approximately 318–350 °C (Zhang et al. 2021a, b). However, we can clearly see that the same reduction process in ZS-derived catalyst (Ha-FeO_x/2ZS) was centered at approximately 265–325 °C, lower than pure Fe_2O_3. Moreover, the following reduction steps show similar characteristic, i.e., the reduction of iron species in ZS-derived catalysts requires obvious lower temperature than that of well crystalized pure FeO_x, firmly conformed the intensive interaction between Fe and impurity atoms in ZS-derived catalysts, which improves the reducibility of iron species, thereby facilitating its LT SCR reactivity. Besides, in Figure S5 and Table S2, ZS sample exhibits only one broad peak at 370–715 °C, and no reduction peak can be observed at lowers temperature, suggestion that the iron species in ZS mainly are mainly Fe_3O_4.

3.2.3 NH_3-TPD

The surface acid sites and acid species of the catalyst were important for promoting the NO conversion. Because sufficient NH_3 adsorption could ensure further SCR reaction. (Sun et al. 2017; Liu et al. 2017a, b). Therefore, the NH_3-TPD experiment was conducted to get more acidity information of ZS-derived catalysts. Generally, the strength and quantity of the catalyst's acid sites can be intuitively reflected by the NH_3 desorption temperature and amounts. At lower temperatures (50–250 °C), the desorption peak was related to the ammonia species physically adsorbed on the material surface and chemisorbed on the weak acid sites (Wang et al. 2020). The peak observed at approximately 350 °C was due to the adsorption of NH_4^+ on medium acid sites. The peak at high temperatures of 400–800 °C was assigned to the desorption of chemical adsorbed ammonia at strong acidic sites (Liu et al. 2017a, b, 2021a, b). In Figure S6, ZS shows three NH_3 desorption peaks at approximately 110, 370 and 530 °C with total acid amount of 1.26 mmol/g. All the ZS-derived catalysts exibit similar TPD curves showing two main NH_3 desorption peaks at around 120 and 350 °C. The NH_3 desorption amounts of the resultant catalysts (> 1.65 mmol/g) are significantly higher than that of raw ZS (1.26 mmol/g), revealing that the acid extraction and alkali precipitation treatment of ZS can effectively improve its surface acidity. Moreover, as shown in Fig. 8, the acid amount of Ha-FeO_x/2ZS is roughly four times more than that of pure FeO_x. Indeed, Zhang et al. (Zhang et al. 2021a, b) found that Nb species introduced into the iron oxide matrix effectively enhances its acid amounts; Sun et
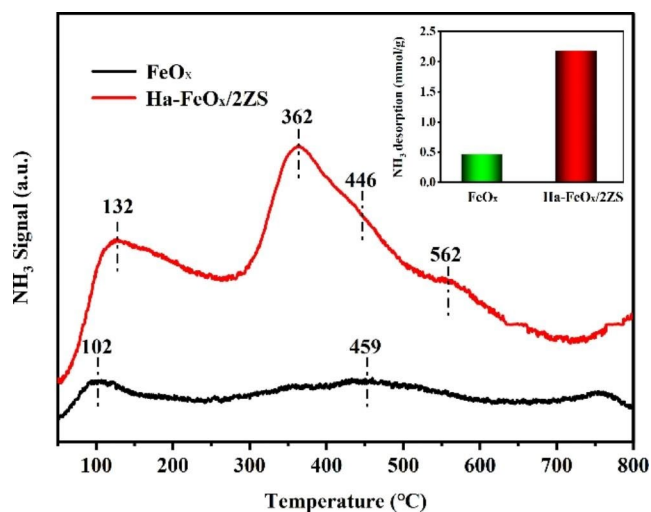
Fig. 8 NH$_3$-TPD patterns of pure FeO$_x$ and Ha-FeO$_x$/2ZS catalyst samples

al. (Sun et al. 2017) also confirmed that the doping of Ti, Al, or Ce into FeO$_x$ can observably boost the surface acidity of resultant catalysts. Therefore, it can be speculated that the higher acid amount of ZS-derived catalysts than that of raw ZS is attributed to the structure regulation of ZS during the acid extraction and alkali precipitation treatment process, while the better surface acidity of the ZS-derived catalysts than pure FeO$_x$ is ascribed to the contribution of heteroatoms which also acquired from the zinc slag.

3.3 In-situ FTIR study over Ha-FeO$_x$/2ZS catalyst

In-situ DRIFT experiments of NH$_3$ adsorption on Ha-FeO$_x$/2ZS at 250 °C were carried out for further understanding the impact of the surface acidity on catalytic reaction. As illustrated in Fig. 9a, when Ha-FeO$_x$/2ZS was persistently exposed to 750 ppm of NH$_3$/N$_2$ flow for 30 min, several IR bands of the adsorbed ammonia species on the catalyst surface emerged in the region of 1000–4000 cm^{-1}, and the peak intensities were enhanced with increasing exposure time. Among them, the bands at 1620, 1281, and 1107 cm^{-1} were identified as the symmetric and asymmetric bending vibration modes of ammonia species absorbed on Lewis acid sites, and the bands at 1691, 1644, and 1392–1512 cm^{-1} were originated from the coordinated NH$_4^+$ on Brønsted acid sites (Guo et al. 2022), while the peaks centered at 3365 and 3267 cm^{-1} is related to the vibration of N-H bonds (Sheng et al. 2018; Liu et al. 2020; Zhu et al. 2021). The peaks emerged at 1344, and 1520–1549 cm^{-1} were assigned to the amide (-NH$_2$) species(Fang et al. 2020). This phenomenon shows that the sufficient acid sites of ZS-derived catalyst ensure abundant adsorbed ammonia species, and they can also be activated simultaneously to improve the NH$_3$-SCR performance.

Figure 9b shows the in-situ DRIFTs spectra of NO + O$_2$ co-adsorption on the as-prepared Ha-FeO$_x$/2ZS catalyst at 250 °C. The nitrates species for gaseous NO$_2$ (1606 cm^{-1}), nitrites (1346 cm^{-1}), monodentate nitrates (1292 and 1564 cm^{-1}) and bidentate nitrates (1514 cm^{-1}) can be

**Fig. 9** In-situ DRIFT spectra of Ha-FeO$_x$/2ZS catalyst exposed to **a** 750 ppm NH$_3$ **b** 750 ppm NO with 5 vol% O$_2$ **c** 750 ppm NO with 5 vol % O$_2$ after NH$_3$ adsorption, and **d** 750 ppm NH$_3$ after NO + O$_2$ adsorption at 250 °C
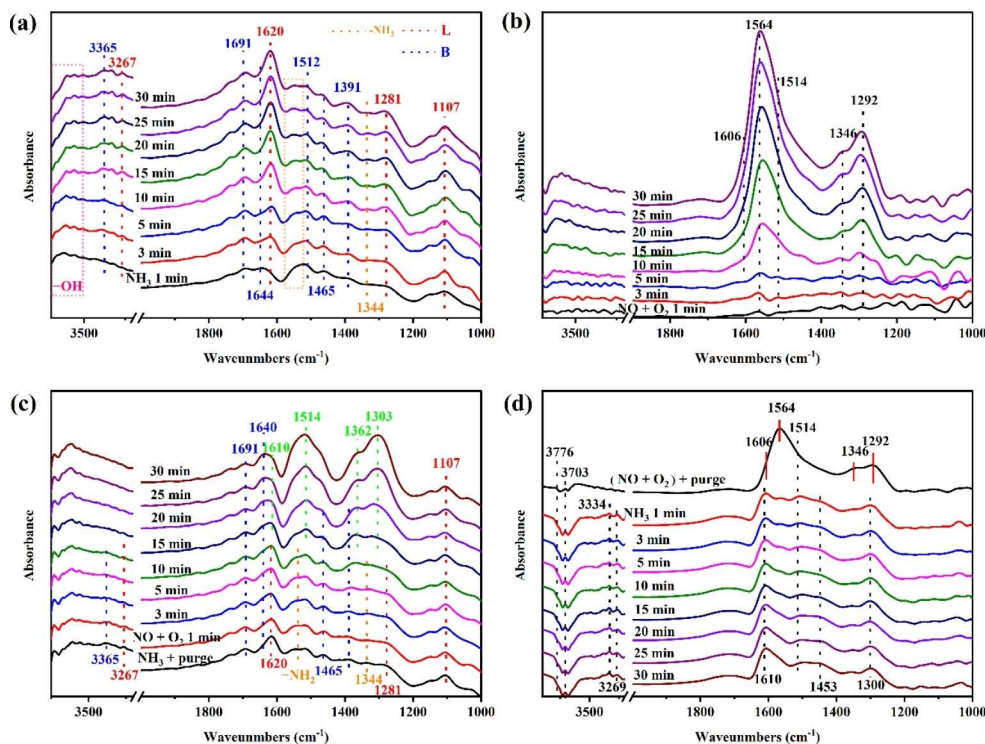
observed with increasing time intervals (Xue et al. 2021). The intensity of monodentate nitrates (1292 and 1564 cm^{-1}) substantially increased after 5 min, suggesting that the NO can be adsorbed and oxidized on the Ha-FeO$_x$/2ZS surface.

Figure 9c shows the in-situ DRIFTS spectra of the interaction between NO+O$_2$ and pre-adsorbed NH$_3$ species at 250 °C over the Ha-FeO$_x$/2ZS catalyst. For Lewis acid sites, the band at 1107 cm^{-1} decreased a little after the introduction of NO+O$_2$, and the bands at 1281 cm^{-1} and 1620 cm^{-1} showed a decrease trend and vanished in 15 min, indicating that the coordinated NH$_3$ species bound to Lewis acid sites were reduced. The band at 1303 cm^{-1} (monodentate nitrates) began to accumulate, which suggested that monodentate nitrates and NH$_3$ reacted through the Langmuir-Hinshelwood (L-H) mechanism at Lewis acid sites. The peak at 1640 cm^{-1} related to gaseous NO$_2$ accumulated gradually at the same time. According to an Eley-Rideal (E-R) mechanism, the gaseous NO$_2$ would interact with the absorbed NH$_3$ species and then accumulate on the catalyst surface. Moreover, the peaks of NH$_3$ adsorbed on the Brønsted acid sites (1392–1512 cm^{-1}) vanished after 20 min, illustrating that Brønsted acid site also took part in the SCR reaction. The bands at 1514 and 1362 cm^{-1} were covered by newly formed peaks and showed a marked increase, which might be due to the accumulation of the nitrate species (Pu et al. 2022). These results illustrate that the NH$_3$-SCR reaction on the Ha-FeO$_x$/2ZS proceeded through both the L-H and E-R mechanisms.
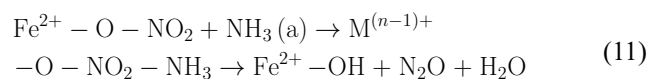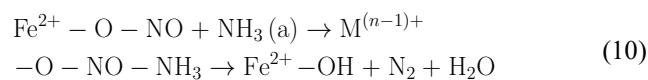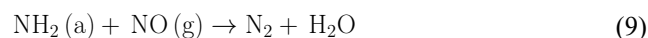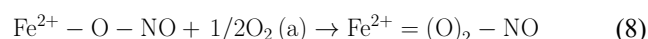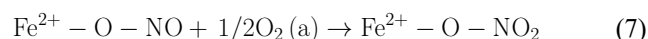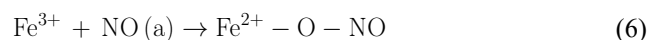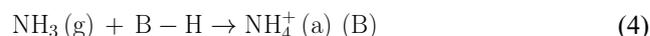
Figure 9d shows the in-situ DRIFTs spectra of the interaction between NH$_3$ and pre-adsorbed NO+O$_2$ at 250 °C. After feeding NH$_3$, only the band at 1514 cm^{-1} belonging to bidentate nitrates was unchanged, while the bands at 1624, 1564, 1346 and 1292 cm^{-1} attributed to gaseous NO$_2$, nitrites and monodentate nitrates rapidly disappeared proving that bidentate nitrates were not the active intermediates,
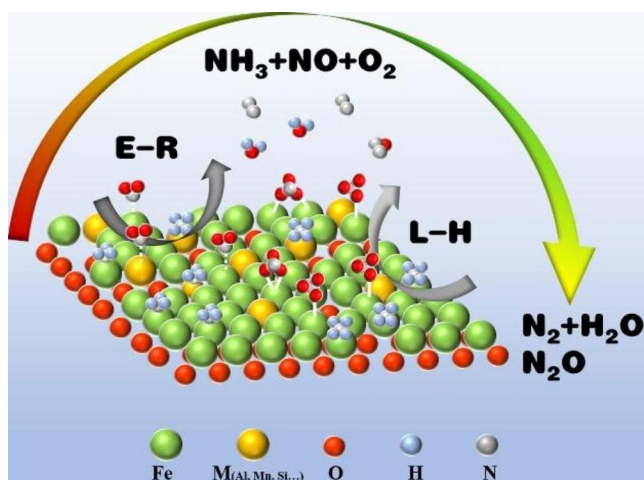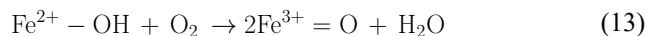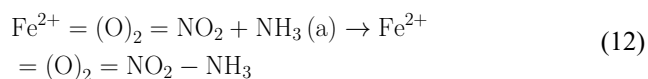
whereas the gaseous NO$_2$, nitrites and monodentate nitrates reacted with NH$_3$ actively. Notably, the NH$_3$ adsorbed on Lewis acid sites at 3334, 3269 and 1610 cm^{-1} and the Brønsted sites at 1453 cm^{-1} can be rapidly observed at the first 1 min when the NO+O$_2$ pre-adsorbed catalysts were exposed to NH$_3$. Compared with Fig. 9c, the rapid reaction between the adsorbed nitrate species and the adsorbed NH$_3$ species firmly suggests that the NO reduction over Ha-FeO$_x$/2ZS easily proceeded via the L-H mechanism, which is the dominant reaction route for NH$_3$-SCR reaction at low temperature over ZS-derived catalysts.

According to above-mentioned results, a possible SCR deNO$_x$ mechanism over Ha-FeO$_x$/2ZS catalysts was proposed as displayed Fig. 10. Firstly, NH$_3$ can be absorbed and activated to be reactive -NH$_2$ and NH$_4^+$ intermediates at Lewis and Brønste acid sites, respectively (Eqs. (3) and (4)). Meanwhile, the heteroatoms in the catalyst improved the amount of oxygen vacancies, promoting the oxidation of physically adsorbed NO by M^{n+} and forming nitrites and nitrates species via Eqs. (6), (7) and (8), which are beneficial for the reaction in Eqs. (10), (11) and (12) (Zhang et al. 2021a, b; Song et al. 2020; Chen et al. 2021). Finally, the activated NH$_3$ and NO$_x$ species are reacted to be N$_2$ and H$_2$O (9)–(12). Moreover, owing to the strong redox interaction between Fe with heteroatoms as shown Eqs. (14), which promotes the reducibility of Fe species at low temperatures, thereby further facilitating its low temperature reactivity.

$$NH_3\,(g) \rightarrow NH_3\,(a) \rightarrow L - NH_2\,(a) \tag{3}$$

$$NH_3\,(g) + B - H \rightarrow NH_4^+\,(a)\,(B) \tag{4}$$

$$NO\,(g) \rightarrow NO\,(a) \tag{5}$$

$$Fe^{3+} + NO\,(a) \rightarrow Fe^{2+} - O - NO \tag{6}$$

$$Fe^{2+} - O - NO + 1/2O_2\,(a) \rightarrow Fe^{2+} - O - NO_2 \tag{7}$$

$$Fe^{2+} - O - NO + 1/2O_2\,(a) \rightarrow Fe^{2+} = (O)_2 - NO \tag{8}$$

$$NH_2\,(a) + NO\,(g) \rightarrow N_2 + H_2O \tag{9}$$

$$Fe^{2+} - O - NO + NH_3\,(a) \rightarrow M^{(n-1)+} \\ -O - NO - NH_3 \rightarrow Fe^{2+} - OH + N_2 + H_2O \tag{10}$$

$$Fe^{2+} - O - NO_2 + NH_3\,(a) \rightarrow M^{(n-1)+} \\ -O - NO_2 - NH_3 \rightarrow Fe^{2+} - OH + N_2O + H_2O \tag{11}$$

Fig. 10 Scheme represents for the NH$_3$-SCR mechanism over the Ha-FeO$_x$/2ZS catalyst

$$Fe^{2+} = (O)_2 = NO_2 + NH_3 (a) \rightarrow Fe^{2+} \tag{12}$$
$$= (O)_2 = NO_2 - NH_3$$

$$Fe^{2+} - OH + O_2 \rightarrow 2Fe^{3+} = O + H_2O \tag{13}$$

$$Fe^{3+} + M^{n+} Fe^{2+} + M^{(n-1)+} \tag{14}$$

Notes: L: Lewis acid sites; B: Brønste acid sites; M: non-ferrous metals

4 Conclusions

In this study, hazardous zinc slag was high value-added utilized to prepare a new type of low-cost and efficient SCR catalyst via a facile sol-gel method. The prepared Ha-FeO$_x$/yZS catalyst exhibited greater than 90% of NO removal efficiency and N$_2$ selectivity, which was obviously superior to the reported pure FeO$_x$, Fe$_9$Ti$_1$O$_x$ and γ-Fe$_2$O$_3$ catalysts. In addition, compared with α-Fe$_2$O$_3$, Fe/Beta and Mn$_{(0.2)}$-FeO$_x$ reported (> 300 °C), the Ha-FeO$_x$/yZS showed better low temperature activity. The characterizations showed that the intensive interactions among Fe and heteroatoms inhibited the crystal growth, leading to the prepared catalyst possessing amorphous morphology with large BET surface area, plenty of adsorbed oxygen species, and abundant acid sites. These characteristics were beneficial for the electron transfer between iron and other metal ions, thus promoting the oxidation-reduction cycle of SCR reaction. In this case, not only the high-content specie Fe in zinc slag was utilized as raw material to prepare the iron oxide-based catalyst, but the low-content species such as Si, Al, Mn, and Zn were also resourced as doped heteroatoms in the iron oxide matrix, and their synergy effect afforded the resultant catalyst exhibiting excellent reactivity. It is a new and efficient method for zinc slag treatment with high added-value, and shows promising application prospects in NO$_x$ removal by NH$_3$-SCR, thereby reaching the goal of treating gas waste with solid waste.

Declarations

Competing interest The authors declare that they have no known competing financial interests or personal relationships that could have appeared to influence the work reported in this paper.

References

Alex T, Kalinkin A, Nath S, Gurevich B, Kalinkina E, Tyukavkina V, Kumar S (2013) Utilization of zinc slag through geopolymerization: influence of milling atmosphere. Int J Miner Process 123:102–107. https://doi.org/10.1016/j.minpro.2013.06.001

Awual MR (2016) Solid phase sensitive palladium (II) ions detection and recovery using ligand based efficient conjugate nanomaterials. Chem Eng J 300:264–272. https://doi.org/10.1016/j.cej.2016.04.071

Awual MR (2017) Novel nanocomposite materials for efficient and selective mercury ions capturing from wastewater. Chem Eng J 307:456–465. https://doi.org/10.1016/j.cej.2016.08.108

Awual MR, Hasan MM (2019) A ligand based innovative composite material for selective lead (II) capturing from wastewater. J Mol Liq 294:111679. https://doi.org/10.1016/j.molliq.2019.111679

Awual MR, Alharthi NH, Okamoto Y, Karim MR, Halim ME, Hasan MM, Rahman MM, Islam MM, Khaleque MA, Sheikh MC (2017a) Ligand field effect for Dysprosium (III) and lutetium (III) adsorption and EXAFS coordination with novel composite nanomaterials. Chem Eng J 320:427–435. https://doi.org/10.1016/j.cej.2017a.03.075

Awual MR, Alharthi NH, Hasan MM, Karim MR, Islam A, Znad H, Hossain MA, Halim ME, Rahman MM, Khaleque MA (2017b) Inorganic-organic based novel nano-conjugate material for effective cobalt (II) ions capturing from wastewater. Chem Eng J 324:130–139. https://doi.org/10.1016/j.cej.2017b.05.026

Awual MR, Hasan MM, Islam A, Rahman MM, Asiri AM, Khaleque MA, Sheikh MC (2019) Offering an innovative composited material for effective lead (II) monitoring and removal from polluted water. J Clean Prod 231:214–223. https://doi.org/10.1016/j.jclepro.2019.05.125

Bersani D, Lottici PP, Montenero A (1999) Micro-Raman Investigation of Iron Oxide Films and Powders produced by Sol-Gel Syntheses. J Raman Spectrosc 30(5):355–360. https://doi.org/10.1002/(SICI)1097-4555(199905)30:5

Chen Z, Wang F, Li H, Yang Q, Wang L, Li X (2011) Low-temperature selective Catalytic reduction of NO$_x$ with NH$_3$ over Fe-Mn mixed-oxide catalysts containing Fe$_3$Mn$_3$O$_8$ phase. Ind Eng Chem Res 51(1):202–212. https://doi.org/10.1021/ie201894c

Chen H, Zhang YJ, He PY, Li CJ (2019) Synthesis, characterization and modification of monolithic ZSM-5 from geopolymer for CO$_2$ capture: experiments and DFT calculations. Energy 179:422–430. https://doi.org/10.1016/j.energy.2019.04.113

Chen Y, Liao Y, Chen L, Chen Z, Ma X (2021) Performance of transition metal (Cu, Fe and Co) modified SCR catalysts for simultaneous removal of NO and volatile organic compounds (VOCs) from coal-fired power plant flue gas. Fuel 289:119849. https://doi.org/10.1016/j.fuel.2020.119849

Chen H, Liu LC, Dong S, Zhang Y, He P (2022) Development of a new type of phosphoric acid based geopolymer/activated carbon composite for selective CO_2 capture. Mater Lett 325:132869. https://doi.org/10.1016/j.matlet.2022.132869

Chen Y, Yan H, Teng W, Li J, Liu W, Ren S, Yang J, Liu Q (2023) Comparative study on N_2O formation pathways over bulk MoO_3 and MoO_3-x nanosheets decorated Fe_2O_3-containing solid waste NH_3-SCR catalysts. Fuel 337:127210. https://doi.org/10.1016/j.apcatb.2013.02.025

Chernyshova IV, Hochella MF Jr, Madden AS (2007) Size-dependent structural transformations of hematite nanoparticles. 1. Phase transition. Phys Chem Chem Phys 9(14):1736–1750. https://doi.org/10.1039/b618790k

Fan Z, Shi JW, Gao C, Gao G, Wang B, Niu C (2017) Rationally Design Porous MnO_x-FeO_x Nanoneedles for low-temperature selective Catalytic reduction of NO_x by NH_3. ACS Appl Mater Interfaces. https://doi.org/10.1021/acsami.7b00739

Fang X, Liu Y, Cen W, Cheng Y (2020) Birnessite as a highly efficient Catalyst for low-temperature NH_3-SCR: the vital role of Surface Oxygen Vacancies. Ind Eng Chem Res 59(33):14606–14615. https://doi.org/10.1021/acs.iecr.0c00188

Fang D, Hou S, Ye Y, Jin Q, He F, Xie J (2022) Insight into highly efficient FeO_x catalysts for the selective catalytic reduction of NO_x by NH_3: experimental and DFT study. Appl Surf Sci 599:153998. https://doi.org/10.1016/j.apsusc.2022.153998

Faria DLA, d, Silva SV, de Oliveira MT (2005) Raman microspectroscopy of some iron oxides and oxyhydroxides. J Raman Spectrosc 28(11): 873–878. https://doi.org/10.1002/(SICI)1097-4555(199711)28:11<873::AID-JRS177>3.0.CO;2-B

Guo M, Liu C, Liu Q, Wang Y, Fan B, Wang H, Liu B, Cui S, Zhao Y (2022) Investigation of SO_2 Resistance on Novel $Cr_{0.8}Zr_{0.2}O_x$ catalysts for Marine Low-Temperature SCR of NO removal. ACS ES&T Engineering 2(10):1825–1835. https://doi.org/10.1021/acsestengg.2c00084

Han L, Gao M, Feng C, Shi L, Zhang D (2019a) Fe2O3-CeO2@ Al2O3 nanoarrays on Al-mesh as SO2-Tolerant Monolith catalysts for NOx reduction by NH3. Environ Sci Technol 53(10):5946–5956. https://doi.org/10.1021/acs.est.9b01217

Han L, Cai S, Gao M, Hasegawa J-y, Wang P, Zhang J, Shi L, Zhang D (2019b) Selective Catalytic Reduction of NOx with NH3 by Using Novel Catalysts: State of the Art and Future Prospects. Chem Rev 119(19):10916–10976. https://doi.org/10.1021/acs.chemrev.9b00202

Hasan MN, Salman MS, Hasan MM, Kubra KT, Sheikh MC, Rehan AI, Rasee AI, Awual ME, Waliullah R, Hossain MS (2023a) Assessing sustainable lutetium (III) ions adsorption and recovery using novel composite hybrid nanomaterials. J Mol Struct 1276:134795. https://doi.org/10.1016/j.molstruc.2022.134795

Hasan MM, Kubra KT, Hasan MN, Awual ME, Salman MS, Sheikh MC, Rehan AI, Rasee AI, Waliullah R, Islam MS (2023b) Sustainable ligand-modified based composite material for the selective and effective cadmium (II) capturing from wastewater. J Mol Liq 371:121125. https://doi.org/10.1016/j.molliq.2022.121125

Kang K, Yao X, Huang Y, Cao J, Rong J, Zhao W, Luo W, Chen Y (2021) Insights into the co-doping effect of Fe^{3+} and Zr^{4+} on the anti-K performance of $CeTiO_x$ catalyst for NH_3-SCR reaction. J Hazard Mater 416:125821. https://doi.org/10.1016/j.jhazmat.2021.125821

Li X, Li J, Peng Y, Zhang T, Liu S, Hao J (2015) Selective catalytic reduction of NO with NH_3 over novel iron-tungsten mixed oxide catalyst in a broad temperature range. Catal Sci Technol 5(9):4556–4564. https://doi.org/10.1039/c5cy00605h

Li Y, Wan Y, Li Y, Zhan S, Guan Q, Tian Y (2016) Low-temperature selective Catalytic reduction of NO with NH_3 over Mn_2O_3-Doped Fe_2O_3 hexagonal microsheets. ACS Appl Mater Interfaces 8(8):5224–5233. https://doi.org/10.1021/acsami.5b10264

Li X, Chen J, Lu C, Luo G, Yao H (2021) Performance of Mo modified γ-Fe_2O_3 catalyst for selective catalytic reduction of NOx with ammonia: presence of arsenic in flue gas. Fuel 294:120552. https://doi.org/10.1016/j.fuel.2021.120552

Liu F, He H (2010) Structure-activity relationship of Iron Titanate catalysts in the selective Catalytic reduction of NO_x with NH_3. J Phys Chem C 40(114):16929–16936. https://doi.org/10.1021/jp912163k

Liu J, Liu J, Zhao Z, Wei Y, Song W (2017a) Fe-Beta@CeO2 core-shell catalyst with tunable shell thickness for selective catalytic reduction of NOx with NH3. AIChE J 63(10):4430–4441. https://doi.org/10.1002/aic.15743

Liu H, Zhang Z, Li Q, Chen T, Zhang C, Chen D, Zhu C, Jiang Y (2017b) Novel Method for Preparing Controllable Nanoporous a-Fe2O3 and its Reactivity to SCR De-NOx. Aerosol Air Qual Res 17(7):1898–1908. https://doi.org/10.4209/aaqr.2017b.05.0188

Liu Z, Sun G, Chen C, Sun K, Zeng L, Yang L, Chen Y, Wang W, Liu B, Lu Y, Pan Y, Liu Y, Liu C (2020) Fe-Doped Mn_3O_4 spinel nanoparticles with highly exposed Feoct-O-Mntet Sites for efficient selective Catalytic reduction (SCR) of NO with Ammonia at Low temperatures. ACS Catal 10(12):6803–6809. https://doi.org/10.1021/acscatal.0c01284

Liu J, Cheng H, Zheng H, Zhang L, Liu B, Song W, Liu J, Zhu W, Li H, Zhao Z (2021a) Insight into the Potassium Poisoning Effect for Selective Catalytic Reduction of NOx with NH3 over Fe/Beta. ACS Catal 11(24):14727–14739. https://doi.org/10.1021/acscatal.1c04497

Liu H, You C, Wang H (2021b) Experimental and Density Functional Theory Studies on the Zeolite-Based Fe-Ni-W Trimetallic Catalyst for High-Temperature NOx Selective Catalytic Reduction: Identification of Active Sites Suppressing Ammonia Overoxidation. ACS Catal 11(3):1189–1201. https://doi.org/10.1021/acscatal.0c03949

Luo W, Rong J, Zhao W, Kang K, Long L, Yao X (2022) Morphology and crystal–plane dependence of CeO_2-TiO_2 catalysts: activity and mechanism for the selective catalytic reduction of NO with NH_3. Chem Eng J 444:136488. https://doi.org/10.1016/j.cej.2022.136488

Morrison C, Hooper R, Lardner K (2003) The use of ferro-silicate slag from ISF zinc production as a sand replacement in concrete. Cem Concr Res 33(12):2085–2089. https://doi.org/10.1016/s0008-8846(03)00234-5

Mu J, Li X, Wang X, Fan S, Yin Z, Li Z, Tadé M, O,Liu S (2020) New insight into the effects of NH_3 on SO_2 poisoning for in situ removal of metal sulfates in low-temperature NH_3-SCR over an Fe-V catalyst. J Phys Chem C 124(39):21396–21406. https://doi.org/10.1021/acs.jpcc.0c04902

Nath SK (2020) Fly ash and zinc slag blended geopolymer: immobilization of hazardous materials and development of paving blocks. J Hazard Mater 387:121673. https://doi.org/10.1016/j.jhazmat.2019.121673

Pan D, Li L, Tian X, Wu Y, Cheng N, Yu H (2019) A review on lead slag generation, characteristics, and utilization. Resour Conserv Recycl 146:140–155. https://doi.org/10.1016/j.resconrec.2019.03.036

Prasad PS, Ramana GV (2016) Imperial smelting furnace (zinc) slag as a structural fill in reinforced soil structures. Geotext Geomembr 44(3):406–428. https://doi.org/10.1016/j.geotexmem.2016.01.009

Pu Y, Yang L, Yao C, Jiang W, Yao L (2022) Low-cost Mn-Fe/SAPO-34 catalyst from natural ferromanganese ore and lithium-silicon-powder waste for efficient low-temperature NH_3-SCR removal of NO_x. Chemosphere 293:133465. https://doi.org/10.1016/j.chemosphere.2021.133465

Qi L, Sun Z, Tang Q, Wang J, Huang T, Sun C, Gao F, Tang C, Dong L (2020) Getting insight into the effect of CuO on red mud for

the selective catalytic reduction of NO by NH_3. J Hazard Mater 396:122459. https://doi.org/10.1016/j.jhazmat.2020.122459

Salman MS, Sheikh MC, Hasan MM, Hasan MN, Kubra KT, Rehan AI, Awual ME, Rasee AI, Waliullah R, Hossain MS (2023) Chitosan-coated cotton fiber composite for efficient toxic dye encapsulation from aqueous media. Appl Surf Sci 622:157008. https://doi.org/10.1016/j.apsusc.2023.157008

Shan W, Geng Y, Chen X, Huang N, Liu F, Yang S (2016) A highly efficient $CeWO_x$ catalyst for the selective catalytic reduction of NO_x with NH_3. Catal Sci Technol 6(4):1195–1200. https://doi.org/10.1039/C5CY01282A

Sheng Z, Ma D, Yu D, Xiao X, Huang B, Yang L, Wang S (2018) Synthesis of novel $MnO@TiO_2$ core-shell nanorod catalyst for low-temperature NH_3-selective catalytic reduction of NO with enhanced SO_2 tolerance. Chin J Catal 39(4):821–830. https://doi.org/10.1016/s1872-2067(18)63059-1

Song S, Sun W, Wang L, Liu R, Han H, Hu Y, Yang Y (2019) Recovery of cobalt and zinc from the leaching solution of zinc smelting slag. J Environ Chem Eng 7(1):102777. https://doi.org/10.1016/j.jece.2018.11.022

Song Z, Wang B, Yang W, Chen T, Ma C, Sun L (2020) Simultaneous removal of NO and SO_2 through heterogeneous catalytic oxidation-absorption process using magnetic $Fe_{2.5}M_{0.5}O_4$ (M = fe, Mn, Ti and Cu) catalysts with vaporized H_2O_2. Chem Eng J 386:123883. https://doi.org/10.1016/j.cej.2019.123883

Sun J, Lu Y, Zhang L, Ge C, Tang C, Wan H, Dong L (2017) Comparative study of different Doped Metal cations on the reduction, acidity, and activity of $Fe_9M_1O_x$ (M = Ti^{4+}, $Ce^{4+/3+}$, Al^{3+}) catalysts for NH_3-SCR reaction. Ind Eng Chem Res 56(42):12101–12110. https://doi.org/10.1021/acs.iecr.7b03080

Twigg MV (2007) Progress and future challenges in controlling automotive exhaust gas emissions. Appl Catal B 70(1–4):2–15. https://doi.org/10.1016/j.apcatb.2006.02.029

Wang P, Yu D, Zhang L, Ren Y, Jin M, Lei L (2020) Evolution mechanism of NO_x in NH_3-SCR reaction over Fe ZSM-5 catalyst: species performance relationships. Appl Catal A 607:117806. https://doi.org/10.1016/j.apcata.2020.117806

Wei L, Li X, Mu J, Wang X, Fan S, Yin Z, Tadé M, O,Liu S (2020) Rationally tailored Redox Properties of a Mesoporous Mn-Fe Spinel nanostructure for boosting low-temperature selective Catalytic reduction of NO_x with NH_3. ACS SusTain Chem Eng 8(48):17727–17739. https://doi.org/10.1021/acssuschemeng.0c05862

Xia M, Muhammad F, Zeng L, Li S, Huang X, Jiao B, Shiau Y, Li D (2019) Solidification/stabilization of lead-zinc smelting slag in composite based geopolymer. J Clean Prod 209:1206–1215. https://doi.org/10.1016/j.jclepro.2018.10.265

Xue H, Guo X, Meng T, Guo Q, Mao D, Wang S (2021) Cu-ZSM-5 Catalyst impregnated with Mn-Co oxide for the selected Catalytic reduction of NO: Physicochemical Property-Catalytic Activity Relationship and In-Situ DRIFTS study for the reaction mechanism. ACS Catal 11(13):7702–7718. https://doi.org/10.1021/acscatal.1c01172

Yang S, Qi F, Xiong S, Dang H, Liao Y, Wong PK, Li J (2016) MnO supported on Fe-Ti spinel: a novel mn based low temperature

SCR catalyst with a high N_2 selectivity. Appl Catal B 181:570–580. https://doi.org/10.1016/j.apcatb.2015.08.023

Yu Y, Tan W, An D, Wang X, Liu A, Zou W, Tang C, Ge C, Tong Q, Sun J, Dong L (2021) Insight into the SO_2 resistance mechanism on γ-Fe_2O_3 catalyst in NH_3-SCR reaction: A collaborated experimental and DFT study. Appl Catal B 281:119544. https://doi.org/10.1016/j.apcatb.2020.119544

Yuan E-H, Li M, Yang M-H, Huang X, Zhang K, Han W, Tang Z, Liu Z-W (2022) Encapsulation of ultra-small Cu-Fe into ZSM-5 zeolites for NH_3-SCR with broad reaction-temperature ranges. Micropor Mesopor Mat 331:111675. https://doi.org/10.1016/j.micromeso.2021.111675

Zhang YJ, Liu LC, Ni L, L,Wang BL (2013) A facile and low-cost synthesis of granulated blast furnace slag-based cementitious material coupled with Fe_2O_3 catalyst for treatment of dye wastewater. Appl Catal B-Environ 138:9–16. https://doi.org/10.1016/j.apcatb.2013.02.025

Zhang J, Huang Z, Du Y, Sánchez-Ochoa F, Wu X, Jing G (2018) Identification of active Sites over Fe_2O_3-Based Architecture: the Promotion Effect of H_2SO_4 Erosion Synthetic Protocol. ACS Appl Energ Mater 1(6):2385–2391. https://doi.org/10.1021/acsaem.8b00353

Zhang K, Wang J, Guan P, Li N, Gong Z, Zhao R, Luo H, Wu W (2020) Low-temperature NH_3-SCR catalytic characteristic of Ce-Fe solid solutions based on rare earth concentrate. Mater Res Bull 128:110871. https://doi.org/10.1016/j.materresbull.2020.110871

Zhang W, Shi X, Yan Z, Shan Y, Zhu Y, Yu Y, He H (2021a) Design of High-Performance Iron-Niobium Composite Oxide Catalysts for NH3-SCR: Insights into the Interaction between Fe and Nb. ACS Catal 11(15):9825–9836. https://doi.org/10.1021/acscatal.1c01619

Zhang Z, Li R, Wang M, Li Y, Tong Y, Yang P, Zhu Y (2021b) Two steps synthesis of CeTiOx oxides nanotube catalyst: Enhanced activity, resistance of SO2 and H2O for low temperature NH3-SCR of NOx. Appl Catal B-Environ 282:119542. https://doi.org/10.1016/j.apcatb.2020.119542

Zhang Q, Cao X, Sun S, Yang W, Fang L, Ma R, Lin C, Li H (2022) Lead zinc slag-based geopolymer: demonstration of heavy metal solidification mechanism from the new perspectives of electronegativity and ion potential. Environ Pollut 293:118509. https://doi.org/10.1016/j.envpol.2021.118509

Zhu X, Zhang L, Dong Y, Ma C (2021) NO2-NH3 SCR over activated Carbon: a combination of NH_4NO_3 formation and consumption. Energy Fuels 35(7):6167–6178. https://doi.org/10.1021/acs.energyfuels.0c03955

Zhu L, Yao J, Ma G, Cao P, Wu S, Li Z (2022) NH_3-SCR performance and SO_2 resistance comparison of CeO_2 based catalysts with Fe/Mo additive surface decoration. Chem Eng J 428:131372. https://doi.org/10.1016/j.cej.2021.131372